Optics Letters

Ptychographic Mueller matrix imaging (PMMI): principle and proof-of-concept demonstration

Ming Gong,[1,2] Li Liu,[3] Jinxiang Du,[3] Bailin Zhuang,[3] Jiamin Liu,[3,6] Honggang Gu,[3,4,5,*] and Shiyuan Liu[1,3,4]

[1]School of Optical and Electronic Information, Huazhong University of Science and Technology, Wuhan 430074, China
[2]Innovation Institute, Huazhong University of Science and Technology, Wuhan 430074, China
[3]State Key Laboratory of Intelligent Manufacturing Equipment and Technology, Huazhong University of Science and Technology, Wuhan 430074, China
[4]Optics Valley Laboratory, Wuhan 430074, China
[5]Guangdong HUST Industrial Technology Research Institute, Guangdong Provincial Key Laboratory of Manufacturing Equipment Digitization, Guangdong 523003, China
[6]jiaminliu@hust.edu.cn
*honggganggu@hust.edu.cn

Received 13 August 2024; revised 8 October 2024; accepted 17 October 2024; posted 21 October 2024; published 5 November 2024

Quantitative characterization of optical anisotropies is extremely important for wide fields and applications. The Mueller matrix, providing all the polarization-related properties of a medium, is a powerful tool for the comprehensive evaluation of optical anisotropies. Here, we propose a ptychographic Mueller matrix imaging (PMMI) technique, which features the Mueller matrix polarization modulation being introduced into the ptychography. The ptychographic reconstruction is performed for each polarization state, and the Mueller matrix can be determined from the reconstructed polarization-modulated amplitude images. A proof-of-concept of the proposed PMMI is implemented, and both simulations and experiments are conducted to demonstrate the validity of the method. Results indicate that the imaging resolution of the home-built PMMI apparatus achieves 1.550 μm at the wavelength of 633 nm, which is of the highest level for the Mueller matrix imaging to the best of our knowledge. A customized birefringent specimen is characterized, and both retardance and axis azimuth are quantitatively evaluated.

https://doi.org/10.1364/OL.539100

Optical anisotropies, including birefringence, dichroism, etc., are universal physical phenomena in both natural and artificial materials, such as biological tissues [1,2], low-dimensional materials [3,4], and liquid crystal polymer [5], making them useful information in clinical diagnosis [6], material analysis [7], and quality monitoring [8]. The Mueller matrix encodes comprehensive polarization-related properties, such as retardance, diattenuation, rotation, and depolarization [9], serving as a powerful tool for quantitatively characterizing optical anisotropies. The primary approach for the Mueller matrix imaging is the Mueller matrix imaging ellipsometers (MMIE), combining ellipsometry with microscopy [10–15]. One major problem for MMIE is that the objective will introduce polarization aberrations [11] and mechanical interference [12,13], which limits the imaging resolution and makes the system bloated and expensive.

Ptychography is a lensless computational imaging technique that addresses the limitations of optical microscopy, eliminating the need for complex compensation of polarization aberrations introduced by objectives. Additionally, it allows simultaneous retrieval of both amplitude and phase [16]. Since conventional ptychography is inadequate to investigate anisotropic materials, several polarization-sensitive ptychographic techniques have been proposed. In general, these techniques can be classified into two categories. The core idea of the first category involves representing an object with Jones matrices and reconstructing them directly by vectorial ptychographical iterative engine (vPIE) [17–19]. It was first reported by Ferrand *et al.* [17] and later extended to the Fourier ptychography (FP) [20]. However, it may face reconstruction ambiguity due to the linear polarization measurement scheme [21]. In addition, Jones matrices fail to comprehensively describe the optical anisotropies especially when the depolarization is present. The second category avoids vPIE and derives the linear retardance and optical axis orientation images from amplitudes reconstructed at different polarization states [22,23]. Currently, methods within the second category are limited to characterizing linear birefringence. Therefore, the main drawback of the above techniques lies in their inability to fully characterize optical anisotropies, which can resort to more powerful Mueller matrix imaging that provides all kinds of polarization-related properties of a medium.

In this Letter, we present a ptychographic Mueller matrix imaging (PMMI) technique to characterize optical anisotropies quantitatively and comprehensively. In the following pages, we will first elucidate the principle underlying the retrieval of Mueller matrix images via a detailed schematic and then implement a proof-of-concept through numerical simulations as well as experiments.

Principle. Figure 1 schematically illustrates the PMMI principle. Figure 1(a) depicts the basic diagram of PMMI, including a

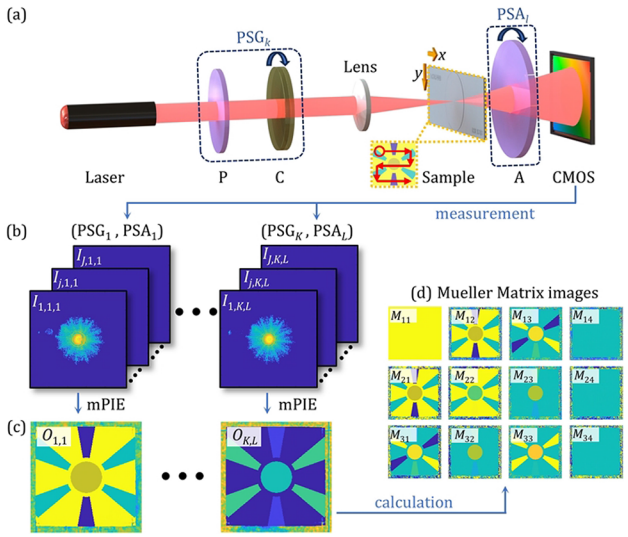

Fig. 1. Principle of the proposed PMMI: (a) Schematic of the PMMI. (b) Recorded diffraction patterns. (c) Reconstructed polarization-modulated amplitude images. (d) Calculated Mueller matrix images. The PSG stands for the polarization state generator, including a fixed polarizer (P) and a rotating compensator (C), and the PSA stands for the polarization state analyzer, including a rotating analyzer (A).

laser, a polarization state generator (PSG), a plano–convex lens, a sample, a polarization state analyzer (PSA), and a detector. The collimated laser light is first modulated into elliptically polarized light by the PSG and then focused as a probe by the lens to interact with the sample. The diffracted light is demodulated by the PSA and recorded by the detector. It is worth pointing out that the configuration of the PSG and PSA is flexible. In Fig. 1(a), a fixed polarizer and a rotating compensator are used as the PSG, and a rotating analyzer as the PSA, facilitating the solvability of 12 Mueller elements. The missing row of the partial Mueller matrix can be analytically determined under additional assumptions [24]. But if we replace the PSA with a rotating compensator and a fixed analyzer, all 16 Mueller elements can be achieved [25]. The subscripts of PSG$_k$ and PSA$_l$ denote the rotation of the compensator and the analyzer to the k-th and l-th azimuth angles, respectively, and $k = 1, 2, \ldots, K$; $l = 1, 2, \ldots, L$. Under each polarization combination of PSG$_k$ and PSA$_l$, the sample is moved along a predetermined trajectory, producing a batch of diffraction patterns after each scan. If there are K PSG states and L PSA states, $K \times L$ batches of diffraction patterns will be captured [Fig. 1(b)], resulting in the reconstruction of $K \times L$ complex images [Fig. 1(c)]. The Mueller matrix images can be derived from the reconstructed polarization-modulated amplitude images [Fig. 1(d)].

The light intensity is first deduced in the ellipsometry formalism:

$$\mathbf{S}_{\text{out}} = \mathbf{A} \cdot \mathbf{M}_{\text{S}} \cdot \mathbf{G}, \tag{1}$$

where $\mathbf{G}$ is a $4 \times K$ matrix for PSG modulation, $\mathbf{A}$ is a $L \times 4$ matrix for PSA demodulation, and $\mathbf{M}_{\text{s}}$ is the 4×4 Mueller matrix of the sample:

$$\mathbf{G} = \begin{bmatrix} \mathbf{G}_1 & \cdots & \mathbf{G}_k & \cdots & \mathbf{G}_K \end{bmatrix}, \tag{2}$$

$$\mathbf{A} = \begin{bmatrix} \mathbf{A}_1 & \cdots & \mathbf{A}_l & \cdots & \mathbf{A}_L \end{bmatrix}^T. \tag{3}$$

In the specific example of Fig. 1(a), $\mathbf{G}_k$ can be expressed as follows:

$$\mathbf{G}_k = \mathbf{R}(-C_k)\mathbf{M}_{\text{C}}(\delta_c)\mathbf{R}(C_k)\mathbf{S}_{\text{in}}, \tag{4}$$

where $\mathbf{S}_{\text{in}} = [1 \ cos2P \ sin2P \ 0]'$ is the Stokes vector of light passing through the polarizer fixed at azimuth P, $\mathbf{R}(C_k)$ is the rotating matrix defining the compensator's axis azimuth C_k, and $\mathbf{M}_{\text{C}}(\delta_c)$ is the Mueller matrix of the compensator with retardance δ_c. $\mathbf{A}_l$ is expressed as follows:

$$\mathbf{A}_l = \begin{bmatrix} 1 & \cos 2A_l & \sin 2A_l & 0 \end{bmatrix}, \tag{5}$$

where A_l stands for the azimuth of the rotating analyzer.

By substituting Eqs. (2)–(5) into Eq. (1), it readily yields the intensity of the forward process. To solve the Mueller matrix, Eq. (1) can be rewritten in the following form:

$$\mathbf{S}_{k,l} = \mathbf{A}_l \cdot \mathbf{M}_{\text{S}} \cdot \mathbf{G}_k = (\mathbf{G}_k^T \otimes \mathbf{A}_l) vec(\mathbf{M}_{\text{S}}), \tag{6}$$

where $vec(\bullet)$ denotes the vectorization operator that transforms the Mueller matrix from a 4×4 matrix to a 16×1 vector and $\otimes$ denotes the Kronecker product operations. When K is larger than 4 and L is larger than 3, respectively, we can construct an overdetermined function to solve the Mueller matrix of the sample:

$$\begin{aligned} \mathbf{S}_{\text{out}} &= \begin{bmatrix} \mathbf{G}_1^T \otimes \mathbf{A}_1 & \cdots & \mathbf{G}_k^T \otimes \mathbf{A}_l & \cdots & \mathbf{G}_K^T \otimes \mathbf{A}_L \end{bmatrix}^T \cdot vec(\mathbf{M}_{\text{S}}) \\ &= \mathbf{D} \cdot vec(\mathbf{M}_{\text{S}}), \end{aligned} \tag{7}$$

where $\mathbf{D}$ is the system matrix of PMMI, related to the parameters P, C_k, δ_c, and A_l. The Mueller matrix can be finally obtained:

$$vec(\mathbf{M}_{\text{s}}) = \mathbf{D}^+ \cdot \mathbf{S}_{\text{out}}, \tag{8}$$

where $(\bullet)^+$ represents the pseudo-inverse.

It should be noted that the deliberations from Eq. (1) to Eq. (8) are within the ellipsometry framework, where the Mueller matrix is determined from the polarization-modulated light intensity. But the raw signals detected in the PMMI are a series of diffraction patterns [Fig. 1(b)], which cannot be directly used for the Mueller matrix imaging using Eq. (8). To address this issue, the ptychography formalism is introduced for the imaging process. The samples in our study are optically thin specimens. Therefore, the wave field on the detector under the polarization state (PSG$_k$, PSA$_l$) is expressed as follows:

$$\Phi_{j,k,l} = \mathcal{F}(O_{j,k,l} \cdot \vec{P}), \tag{9}$$

where $\vec{P}$ and $O_{j,\,k,\,l}$ represent, respectively, the polarized probe and complex amplitude of the object under the polarization state (PSG$_k$, PSA$_l$) at the j-th scanning position and $\mathcal{F}$ denotes the Fourier transform operation, describing the Fraunhofer propagation. The diffractive patterns recorded by the detector are given by $I_{j,\,k,\,l} = |\,\Phi_{j,\,k,\,l}\,|^2$.

In the inverse process, we adopt the momentum ptychographical iterative engine (mPIE) [26] for phase retrieval, reconstructing the complex amplitude of $O_{k,l}$. More details about the mPIE are in Supplement 1. $O_{1,\,1}$ to $O_{K,\,L}$ contain all polarization modulation information. Finally, $|O_{k,l}|^2$ can effectively substitute for $S_{k,\,l}$ in Eqs. (6)–(8) for the computation of the Mueller matrix images:

$$vec(\mathbf{M}_{\text{S}}) = \mathbf{D}^+ \cdot |\mathbf{O}|^2. \tag{10}$$

Results. To verify the PMMI method, both numerical simulations and experiments are performed. In the simulations, three

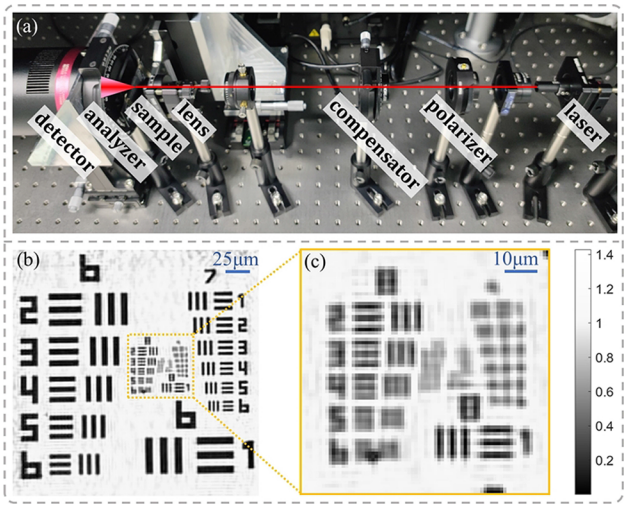

Fig. 2. (a) Home-built apparatus of PMMI. (b) Reconstructed image of the USAF-1951 resolution target. (c) Zoomed-in image of (b).

types of specimens are investigated. The Mueller matrix images, as well as polarization-related properties of these specimens, are successfully retrieved through the proposed method. Details are provided in Supplement 1. For experiments, a home-built apparatus is constructed as a proof of concept as shown in Fig. 2(a). Further configurations are in Supplement 1.

The imaging resolution of PMMI can be approximated by $\lambda \times Z/L$, where λ is the light source wavelength, Z is the distance from the object to the detector, and L is the length of the shorter side of the CMOS sensor. In the home-built PMMI, λ is 633 nm, Z is 37 mm, and L is 15.4 mm. Thus, the expected resolution is about 1.521 μm. To demonstrate the performances of the home-built PMMI apparatus, the USAF-1951 resolution target (from Newport, RES-1) and a customized birefringent specimen (from LBTEK) are tested.

The reconstructed images in Figs. 2(b) and 2(c) show that Group 8-3 can be clearly resolved, indicating a lateral imaging resolution of 1.550 μm for the home-built PMMI, which is highly consistent with the expected value. To the best of our knowledge, the commercially available MMIE claims a lateral resolution of 1 μm. Therefore, the home-built PMMI apparatus achieves the highest level of lateral resolution for the Mueller matrix imaging.

A birefringent pattern of "HUST" was designed and fabricated from LEBTEK by laser direct writing technology. The specialized pattern in the specimen is achieved by controlling the orientation of the fast axis of liquid crystal molecules. The specimen is essentially a linear retarder and exhibits a uniform retardance of 180°. The designed axis azimuths for "H," "U," "S," and "T" are 120°, 150°, 0°, and 30°, respectively. More details about the design information of the specimen can be found in Supplement 1. The birefringent pattern cannot be observed under a normal optical microscope [Fig. 3(a)], nor can it be seen by the conventional ptychography that is insensitive to the optical anisotropies. However, it can be clearly confirmed by a commercial polarizing microscope [Fig. 3(b)] and the home-built PMMI apparatus [Fig. 3(c)].

Figure 4 shows the Mueller matrix images recovered from the reconstructed polarization-modulated amplitudes [Fig. S4, Supplement 1] and distributions of the linear retardance and fast axis azimuth. The 12 Mueller matrix elements normalized

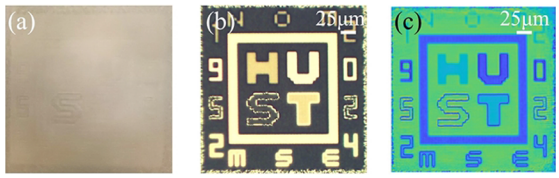

Fig. 3. Images of the customized "HUST" birefringent specimen under (a) optical microscope, (b) polarizing microscope, and (c) home-built PMMI apparatus.

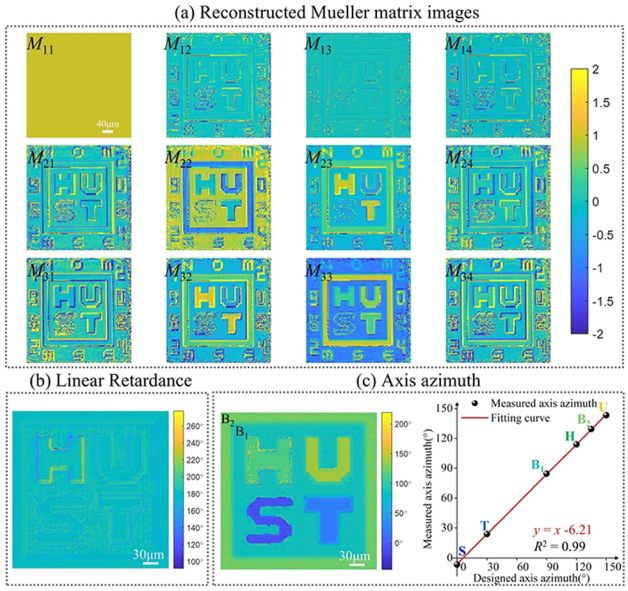

Fig. 4. (a) Reconstructed Mueller matrix images from M_{11} to M_{34} of the "HUST" birefringent specimen using PMMI. (b) Calculated linear retardance of the specimen. (c) Calculated axis azimuth of the specimen.

to M_{11} are determined by the proposed PMMI. The elements M_{12}, M_{13}, M_{14}, M_{21}, and M_{31} are close to zero, matching their theoretical values [Eq. (S1), Supplement 1]. Additionally, M_{24} and M_{34} are near zero, and M_{22} is the inverse of M_{33}, indicating a retardance of about 180°. The linear retardance and axis azimuth can be further calculated from the Mueller matrix, as shown in Figs. 4(b) and 4(c). The average measured linear retardance is 181.61°, aligning with the design value of 180°. The measured average axis azimuths for "H," "U," "S," "T," Background B1, and B2 are 114.06°, 143.26°, −6.56°, 23.89°, 84.59°, and 129.35°, deviating from their design values (120°,150°,0°, 30°, 90°, and 135°) by 5.94°, 6.74°, 6.56°, 6.11°, 5.41°, and 5.65°, respectively. As shown in Fig. 4(c), the high linearity between the measured results and the designed values indicates the validity of PMMI in determining the fast axis azimuth of linear birefringence. The y-intercept of −6.21° is mainly due to the manufacturing misalignment. The fast axis azimuth also contains a random error within the range of ±0.3° due to the noise in controlling the orientation of liquid crystal molecules, according to the supplier [27].

Figure 5 clearly illustrates how the practical axis azimuths θ deviates from the ideal values θ_0. The yellow ellipses represent the liquid crystal molecules, whose arrangement determines the axis azimuths. Ideally, as depicted in Fig. 5(a), the axis azimuth

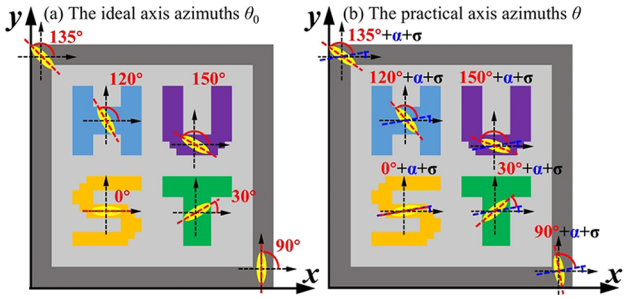

Fig. 5. (a) Designed ideal axis azimuths of the "HUST" specimen. (b) Practical axis azimuths due to the misalignment α and manufacturing error σ.

of 0° should align with the x axis. However, misalignments during manufacturing cause all azimuths to deviate by an angle α from their ideal positions. Additionally, the position precision, σ, reflects the manufacturing error. Thus, the practical axis azimuths of different areas, shown in Fig. 5(b), are expressed as $\theta = \theta_0 + \alpha + \sigma$.

The unusual values at the edges of these letters and background indicate a transition region of ~5 μm between adjacent areas due to the manufacturing process. The region may cause abnormal Mueller matrix values and impact the resolution. Advanced techniques, such as super-resolution algorithm, could potentially mitigate this issue.

Summary. In summary, we proposed a novel PMMI technique for the comprehensive characterization of optical anisotropies. The basic principle of PMMI was elucidated by combining the Mueller matrix ellipsometry framework with ptychographic imaging. The mPIE-reconstructed amplitudes under different polarization states are used to recover the Mueller matrix images of the sample. Both numerical simulations and experiments verified the method. Simulations on different anisotropic specimens indicate that the PMMI is capable of quantitatively and comprehensively characterizing complex optical anisotropies. A proof-of-concept experiment was conducted with a home-built PMMI apparatus, achieving a lateral imaging resolution of 1.550 μm at 633 nm, which is the highest level for the Mueller matrix imaging. Finally, a customized birefringent sample with a "HUST" pattern was characterized by the PMMI, and both the linear retardance and its axis azimuth distribution determined from the measured Mueller matrix images are highly consistent with their designed values. The proposed PMMI method is a powerful tool to characterize micro-distributed anisotropies and can be expected to be applied in various fields, such as low-dimensional materials, metamaterials, and biological issues. However, it faces challenges when dealing with featureless or weak-feature samples, which will be a key focus of future research.

Funding. National Key Research and Development Program of China (2022YFB2803900); National Natural Science Foundation of China (52130504, 52305577); Key Research and Development Program of Hubei Province (2021BAA013); Basic and Applied Basic Research Foundation of Guangdong Province (2023A1515030149); Innovation Project of Optics Valley Laboratory (OVL2023PY003); Interdisciplinary Research Program of Huazhong University of Science and Technology (2023JCYJ047).

Disclosures. H. Gu claims a C.N. patent on the presented PMMI method through Huazhong University of Science and Technology.

Data availability. Data underlying the results presented in this Letter are not publicly available at this time but may be obtained from the authors upon reasonable request.

Supplemental document. See Supplement 1 for supporting content.

REFERENCES

1. C. Li, S. Chen, M. Klemba, *et al.*, J. Biomed. Opt. **21**, 090501 (2016).
2. N.-J. Jan, J. L. Grimm, H. Tran, *et al.*, Biomed. Opt. Express **6**, 4705 (2015).
3. Z. Guo, H. Gu, Y. Yu, *et al.*, Adv. Opt. Mater. **12**, 2303138 (2024).
4. Y. Zhou, Z. Guo, H. Gu, *et al.*, Nat. Photonics **18**, 922 (2024).
5. Y. Wu, Y. Yang, T. Li, *et al.*, Appl. Phys. Lett. **117**, 263301 (2020).
6. C. He, H. He, J. Chang, *et al.*, Light: Sci. Appl. **10**, 194 (2021).
7. Z. Guo, H. Gu, M. Fang, *et al.*, ACS Mater. Lett. **3**, 525 (2021).
8. J.-T. Zettler, Prog. Cryst. Growth Charact. Mater. **35**, 27 (1997).
9. S.-Y. Lu and R. A. Chipman, J. Opt. Soc. Am. A **13**, 1106 (1996).
10. O. Arteaga, M. Baldrís, J. Antó, *et al.*, Appl. Opt. **53**, 2236 (2014).
11. C. Chen, X. Chen, H. Gu, *et al.*, Meas. Sci. Technol. **30**, 025201 (2019).
12. C. Chen, X. Chen, C. Wang, *et al.*, Opt. Express **29**, 32712 (2021).
13. S. Funke, B. Miller, E. Parzinger, *et al.*, J. Phys.: Condes. Matter **28**, 385301 (2016).
14. Y. Wang, H. He, J. Zhang, *et al.*, J. Biomed. Opt. **21**, 071112 (2016).
15. J. Chang, H. He, Y. Wang, *et al.*, J. Biomed. Opt. **21**, 056002 (2016).
16. J. M. Rodenberg and H. M. L. Faulkner, Appl. Phys. Lett. **85**, 4795 (2004).
17. P. Ferrand, M. Allain, and V. Chamard, Opt. Lett. **40**, 5144 (2015).
18. P. Ferrand, A. Baroni, M. Allain, *et al.*, Opt. Lett. **43**, 763 (2018).
19. A. Baroni, M. Allain, P. Li, *et al.*, Opt. Express **27**, 8143 (2019).
20. X. Dai, S. Xu, X. Yang, *et al.*, Biomed. Opt. Express **13**, 1457 (2022).
21. P. Ferrand and M. Mitov, Opt. Lett. **48**, 5081 (2023).
22. S. Song, J. Kim, S. Hur, *et al.*, ACS Photonics **8**, 158 (2021).
23. M. G. Mayani, K. R. Tekseth, D. W. Breiby, *et al.*, Opt. Express **30**, 39891 (2022).
24. H. Fujiwara, *Spectroscopic Ellipsometry: Principles and Applications* (John Wiley & Sons, 2007), Chap. 4.
25. O. Arteaga and R. Ossikovski, J. Opt. Soc. Am. A **36**, 416 (2019).
26. A. Maiden, D. Johnson, and P. Li, Optica **4**, 736 (2017).
27. LBTEK, "Customized diffractive optical element," 2024, https://www.lbtek.com/product/276.html.

Supplemental Document

Optics Letters

Ptychographic Mueller matrix imaging (PMMI): principle and proof-of-concept demonstration: supplement

MING GONG,[1,2] LI LIU,[3] JINXIANG DU,[3] BAILIN ZHUANG,[3] JIAMIN LIU,[3,6] HONGGANG GU,[3,4,5,*] AND SHIYUAN LIU[1,3,4]

[1] *School of Optical and Electronic Information, Huazhong University of Science and Technology, Wuhan 430074, China*
[2] *Innovation Institute, Huazhong University of Science and Technology, Wuhan 430074, China*
[3] *State Key Laboratory of Intelligent Manufacturing Equipment and Technology, Huazhong University of Science and Technology, Wuhan 430074, China*
[4] *Optics Valley Laboratory, Wuhan 430074, China*
[5] *Guangdong HUST Industrial Technology Research Institute, Guangdong Provincial Key Laboratory of Manufacturing Equipment Digitization, Guangdong 523003, China*
[6] *jiaminliu@hust.edu.cn*
[*] *honggganggu@hust.edu.cn*

Supplement DOI: https://doi.org/10.6084/m9.figshare.27268116

Parent Article DOI: https://doi.org/10.1364/OL.539100

(0.1)

Supplemental information

Ptychographic Mueller matrix imaging (PMMI): principle and proof-of-concept demonstration

Ming Gong,[1,2] Li Liu,[3] Jinxiang Du[3], Bailin Zhuang[3], Jiamin Liu[3,6], Honggang Gu[3,4,5,7], and Shiyuan Liu[1,3,4]

[1]*School of Optical and Electronic Information, Huazhong University of Science and Technology, Wuhan 430074, China*
[2]*Innovation Institute, Huazhong University of Science and Technology, Wuhan 430074, China*
[3]*State Key Laboratory of Intelligent Manufacturing Equipment and Technology, Huazhong University of Science and Technology, Wuhan 430074, China*
[4]*Optics Valley Laboratory, Wuhan 430074, China*
[5]*Guangdong HUST Industrial Technology Research Institute, Guangdong Provincial Key Laboratory of Manufacturing Equipment Digitization, Guangdong 523003, China;*
[6]e-mail: jiaminliu@hust.edu.cn;
[7]e-mail: honggganggu@hust.edu.cn

1. Numerical simulations of PMMI

In order to verify the principle of PMMI, numerical simulations are conducted. The simulated experimental apparatus is shown in Fig. 1(a). The laser wavelength is 633 nm. A stationary polarizer, with its transmission axis parallel to the x axis, and a rotating quarter-wave plate are situated within the PSG. Additionally, a rotating analyzer is employed within the PSA. The detector has a pixel count of 4096 × 4096, with a pixel size of 3.76 μm × 3.76 μm. The distance from the object to the detector is set to 50 mm.

1.1 A specimen with pure birefringence

First, we simulate a birefringent object of 768 × 768 pixels. Fig. S1(a) shows the pattern of the object. Each pixel of the object can be determined by Eq. (S1),

$$\mathbf{M}=\begin{bmatrix}1 & 0 & 0 & 0\\ 0 & \cos^2 2\theta+\cos\delta\sin^2 2\theta & (1-\cos\delta)\cos 2\theta\sin 2\theta & \sin\delta\sin 2\theta\\ 0 & (1-\cos\delta)\cos 2\theta\sin 2\theta & \cos\delta\cos^2 2\theta+\sin^2 2\theta & -\sin\delta\cos 2\theta\\ 0 & -\sin\delta\sin 2\theta & \sin\delta\cos 2\theta & \cos\delta\end{bmatrix}, \tag{S1}$$

Here θ represents the fast axis orientation and δ represents the retardance. There are six annularly distributed sector patterns marked with ①~⑥ clockwise on the object. The six patterns have the same retardance of π/2, but their fast axis orientations are set to 45°, 85°, 135°, -135°, -85° and -45° respectively. The background has the retardance of π/6 and the fast axis orientation of 30°. Fig. S1(b) represents the true value of the object's Mueller matrix.

Figure. S1(c) shows the forward numerical simulation. In PSG, the transmission axis of the stationary polarizer is fixed at 0°, while the fast axis of the quarter-wave plate is set to five different angles, C∈{0°, 20°, 40°, 60°, 80°}. In other words, five probes were simulated with distinct polarization states. Each probe is a 256 × 256 pixel Gaussian beam. In PSA, the transmission axis of the analyzer is set to four different angles, A∈{0°, 45°, 90°, 135°}. Hence, there are twenty polarization combinations, ensuring the solvability of the Mueller matrix. For each combination, the object is scanned to generate a batch of diffraction fields. The raster grid

scanning trajectory consists of 255 points, and the scanning step size is 28 pixels, with a 15% random offset to avoid image artefacts. Then the mPIE was ran for every batch of diffraction fields. As a result, twenty reconstructed complex images are obtained as shown in Fig. S1(d). It is observed that the periphery of the image contains a ring of random noise, approximately 50 pixels wide. This occurs because the scanning side length is about 400 pixels, which fails to encompass the entire object. The square of the recovered amplitude can substitute $\mathbf{S}_{out}$ in Eq. (9), and the system matrix **D** can be calculated according to Eq. (8). The reconstructed Mueller matrix images in Fig. S1(e) are in excellent agreement with the first three rows of the true values in Fig. S1(b). This effectively demonstrates the accuracy of the PMMI method.

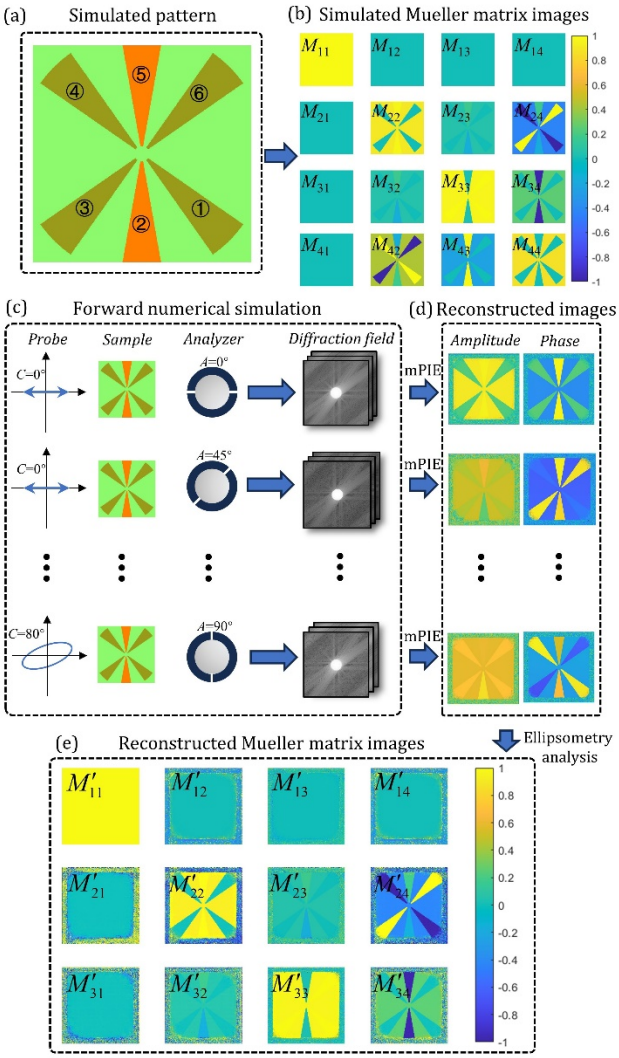

Fig. S1. The process of the numerical simulation. (a) The simulated pattern of a specimen with pure birefringence. (b) The simulated Mueller matrix images. (c) The forward numerical simulation that depicts the propagation of light. (d) The reconstructed complex images by mPIE. (e) The reconstructed Mueller matrix images after ellipsometry analysis.

1.2 A specimen with separated birefringence and dichroism

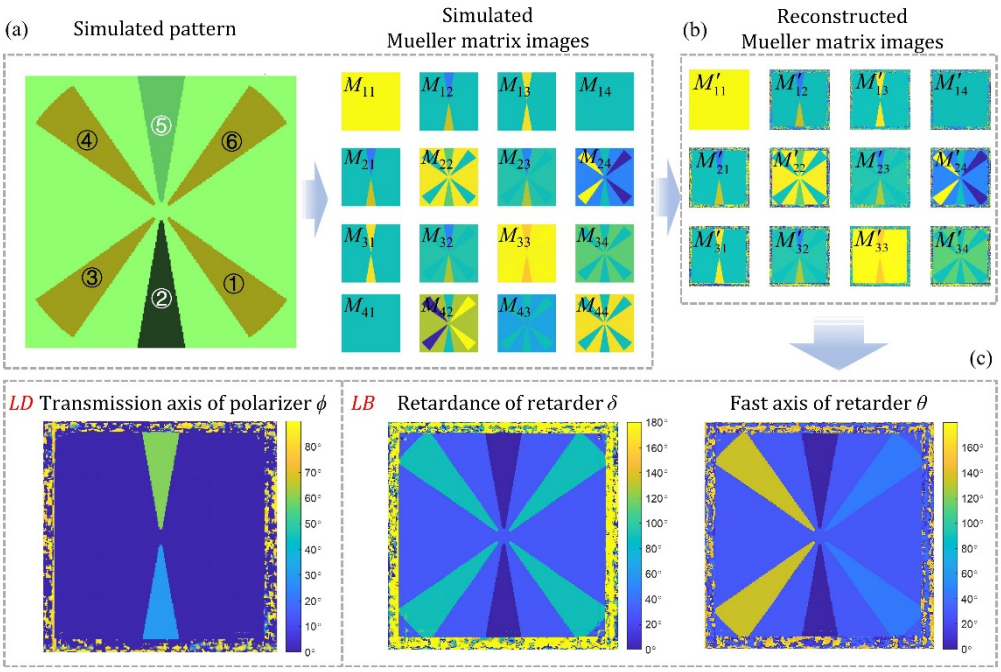

Fig. S2. (a) The simulated pattern and Mueller matrix images of a spicemen with separated birefringence and dichroism. (b) The reconstruced Mueller matrix images. (c) The deduced properties of linear dichroism (LD) and linear birefrigence (LB) from the Mueller matrix.

Then, a specimen with separated birefringence and dichroism is simulated as shown in Fig. S2(a). The object also has six annularly distributed sector patterns marked with ① ~ ⑥. Patterns ①, ③, ④, ⑥ and the background are birefringent, functioning as retarders. While patterns ② and ⑤ exhibit dichroism, acting as polarizers. The retardance is π/2 for patterns ①, ③, ④, ⑥, and π/6 for the background. The fast axis orientation is 45° for patterns ① and ⑥, 135° for patterns ③ and ④, and 30° for the background. The transmission axis orientation is 30° for pattern ② and 60° for pattern ⑤. The Mueller matrix for retarders can be determined by Eq. (S1), while the Mueller matrix for a linear polarizer can be determined by the following expressions,

$$\mathbf{M} = \begin{bmatrix} 1 & \cos 2\phi & \sin 2\phi & 0 \\ \cos 2\phi & \cos^2 2\phi & \sin 2\phi \cos 2\phi & 0 \\ \sin 2\phi & \sin 2\phi \cos 2\phi & \sin^2 2\phi & 0 \\ 0 & 0 & 0 & 0 \end{bmatrix}, \tag{S2}$$

where ϕ stands for the transmission axis orientation. The simulated Mueller matrix images are shown in the right part of Fig. S2(a). The Mueller matrices of patterns ② and ⑤ are Hermitian matrix, indicating the linear dichroism (LD) property. While The Mueller matrices of patterns ①, ③, ④, and ⑥ are unitary matrix, indicating the linear birefringence (LB) property. The configuration of the simulated experimental apparatus is the same as in Section 1.1.

The reconstructed Mueller matrix images are presented in Fig. S2(b). The transmission axis orientation of polarizers ϕ, the retardance δ and fast axis orientation θ of retarders [Fig. S2(c)] are deduced from reconstructed Mueller matrix images. The calculated values are highly consisted with the true values.

1.3 A specimen with integrated birefringence and dichroism

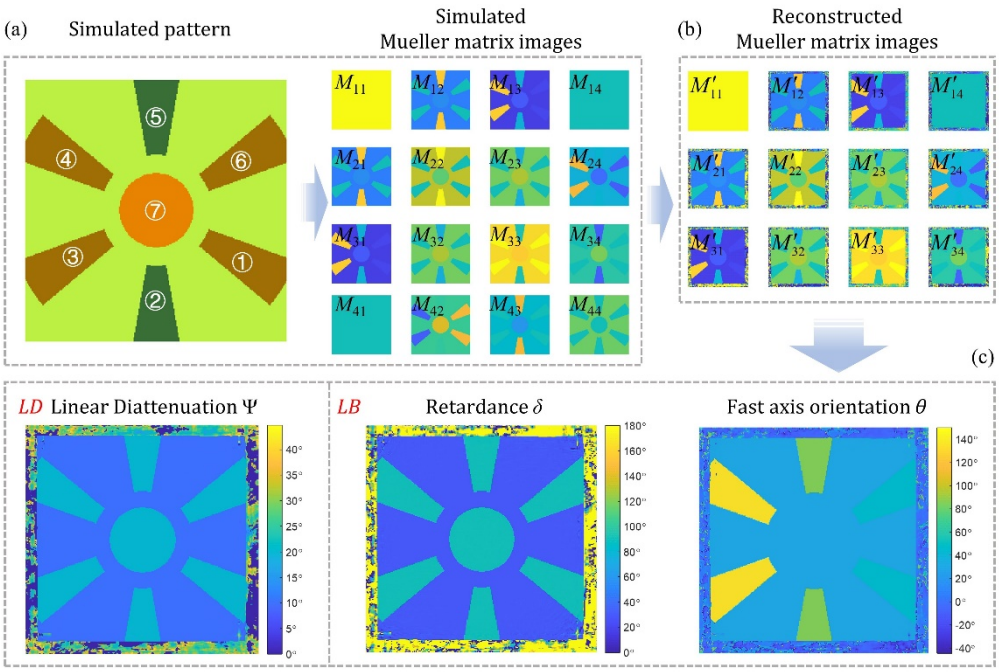

Fig. S3. (a) The simulated pattern and Mueller matrix images of a spicemen with integrated birefringence and dichroism. (b) The reconstruced Mueller matrix images. (c) The deduced properties of linear dichroism (LD) and linear birefrigence (LB) from the Mueller matrix.

Subsequently, a specimen with integrated birefringence and dichroism is simulated as shown in Fig. S3(a). The object has a sun shape. All patterns (① ~ ⑦) and the background exhibit both birefringence and dichroism. Additionally, the axis of birefringence and dichroism are aligned. The diattenuation is described by $\Psi = \tan^{-1}(T_x/T_y)$, where T_x and T_y denote the amplitude transmittance of x and y axis, respectively. The diattenuation is 10° for patterns ① ~ ⑦, and 20° for the background. The retardance is $\pi/2$ for patterns ① ~ ⑦, and $\pi/6$ for the background. The fast axis orientation is 45° for patterns ① and ⑥, 135° for patterns ③ and ④, 85° for patterns ② and ⑤, and 30° for the background. The Mueller matrix of the object can be determined by the following expression:

$$\mathbf{M} = \begin{bmatrix} 1 & -\cos(2\Psi)\cos 2\theta & -\cos(2\Psi)\sin 2\theta & 0 \\ -\cos(2\Psi)\cos 2\theta & \cos^2 2\theta + \sin^2 2\theta \sin(2\Psi)\cos\delta & \sin 2\theta \cos 2\theta[1-\sin(2\Psi)\cos\delta] & \sin 2\theta \sin(2\Psi)\sin\delta \\ -\cos(2\Psi)\sin 2\theta & \sin 2\theta \cos 2\theta[1-\sin(2\Psi)\cos\delta] & \sin^2 2\theta + \cos^2 2\theta \sin(2\Psi)\cos\delta & -\cos 2\theta \sin(2\Psi)\sin\delta \\ 0 & \sin 2\theta \sin(2\Psi)\sin\delta & \cos 2\theta \sin(2\Psi)\sin\delta & \sin(2\Psi)\cos\delta \end{bmatrix}. \tag{S3}$$

where Ψ represents diattenuation, δ represents retardance, and θ represents fast axis orientation. The configuration of the simulated experimental apparatus is also the same as in Section 1.1.

The reconstructed Mueller matrix images are presented in Fig. S3(b). The diattenuation Ψ, the retardance δ and fast axis orientation θ [Fig. S3(c)] are deduced from reconstructed Mueller matrix images. The calculated values are highly consisted with the true values.

2. The algorithm of mPIE

In a ptychography imaging microscope, an "object" is illuminated by a localized "probe" and is driven by a translation stage along a predetermined trajectory, thus forming a series of diffraction field signals. At the j-th scanning position, the diffraction field signal $\boldsymbol{I}_j(\boldsymbol{u})$ recorded by the detector can be expressed by:

$$I_j(\boldsymbol{u}) = \left| \mathcal{F}\left[\mathbf{P}\left(\boldsymbol{r} - \boldsymbol{R}_j\right)\mathbf{O}\left(\boldsymbol{r}\right)\right]\right|^2, \tag{S4}$$

Where $\boldsymbol{r}$ and $\boldsymbol{u}$ are coordinate variables in the real domain and frequency domain respectively. $\mathcal{F}$ is the optical field propagation model and $\boldsymbol{R}_j$ is the scanning shift (x_j, y_j) between the "object" $\boldsymbol{O}(\boldsymbol{r})$ and the "probe" $\boldsymbol{P}(\boldsymbol{r})$. According to the real-space overlap constraints and the reciprocal-space modulus constraints, the ptychographic phase retrieval minimizes the Euclidean norm $\boldsymbol{\varepsilon}$ as [1]:

$$\varepsilon = \arg \min_{\mathbf{P}(\boldsymbol{r}-\boldsymbol{R}_j),\mathbf{O}(\boldsymbol{r})} \sum_j \left\| \sqrt{\boldsymbol{I}_j(\boldsymbol{u})} - \left| \mathcal{F}\left[\mathbf{P}\left(\boldsymbol{r} - \boldsymbol{R}_j\right)\mathbf{O}\left(\boldsymbol{r}\right)\right]\right| \right\|^2, \tag{S5}$$

The detailed iterative process of the ptychographic reconstruction algorithm can be described as follows:

1) The detector collects the raw coherent diffraction signals $\boldsymbol{I}_j(\boldsymbol{u})$ in all scanning positions.
2) Initial guess of the "object" $\mathbf{O}(\boldsymbol{r})$ and the localized "probe" $\boldsymbol{P}(\boldsymbol{r})$.
3) The interaction between the "object" and the localized "probe" generates exit-waves $\boldsymbol{\psi}(\boldsymbol{r})$ in $\boldsymbol{R}_j$:

$$\boldsymbol{\psi}\left(\boldsymbol{r}\right) = \mathbf{P}\left(\boldsymbol{r} - \boldsymbol{R}_j\right)\mathbf{O}\left(\boldsymbol{r}\right), \tag{S6}$$

4) Exit-waves propagate to the detector to generate the guessed diffraction field:

$$\boldsymbol{\Phi}\left(\boldsymbol{u}\right) = \mathcal{F}\left[\boldsymbol{\psi}(\boldsymbol{r})\right], \tag{S7}$$

5) Modulus constraints: replace the estimated amplitude of $\Phi(\boldsymbol{u})$ with the measured diffraction field, while the phase is remained. The updated diffraction signals $\boldsymbol{\Phi'}(\boldsymbol{u})$ can be expressed as:

$$\boldsymbol{\Phi}'(\boldsymbol{u}) = \sqrt{\boldsymbol{I}_j(\boldsymbol{u})}\frac{\boldsymbol{\Phi}(\boldsymbol{u})}{\left|\boldsymbol{\Phi}(\boldsymbol{u})\right|}, \tag{S8}$$

6) The updated diffraction signals are propagated backward to the plane of the object, the updated exit-waves $\boldsymbol{\psi'}(\mathbf{u})$ can be expressed as:

$$\boldsymbol{\psi}'(\boldsymbol{r}) = \mathcal{F}^{-1}\left[\boldsymbol{\Phi}'(\boldsymbol{u})\right], \tag{S9}$$

7) Update the "object" and "probe" according to the difference between estimated exit-waves $\boldsymbol{\psi}(\boldsymbol{r})$ and updated exit-waves $\boldsymbol{\psi'}(\boldsymbol{u})$:

$$\begin{aligned} \mathbf{O}_{j+1}(\boldsymbol{r}) &= \mathbf{O}_j\left(\boldsymbol{r}\right) + \beta_1 \frac{\mathbf{P}_j^*(\boldsymbol{r}-\boldsymbol{R}_j)}{\alpha\left|\mathbf{P}_j(\boldsymbol{r}-\boldsymbol{R}_j)\right|_{\max}^2 + (1-\alpha)\left|\mathbf{P}_j(\boldsymbol{r}-\boldsymbol{R}_j)\right|^2}\left(\boldsymbol{\psi}'(\boldsymbol{r}) - \boldsymbol{\psi}\left(\boldsymbol{r}\right)\right), \\ \mathbf{P}_{j+1}(\boldsymbol{r}-\boldsymbol{R}_j) &= \mathbf{P}_j\left(\boldsymbol{r}-\boldsymbol{R}_j\right) + \beta_2 \frac{\mathbf{O}_j^*(\boldsymbol{r}-\boldsymbol{R}_j)}{\alpha\left|\mathbf{O}_j(\boldsymbol{r})\right|_{\max}^2 + (1-\alpha)\left|\mathbf{O}_j(\boldsymbol{r})\right|^2}\left(\boldsymbol{\psi}'(\boldsymbol{r}) - \boldsymbol{\psi}\left(\boldsymbol{r}\right)\right) \end{aligned} \tag{S10}$$

where α is the turning parameter and β is the step size.

8) Repeat steps 3-7 T times.

9) Adding momentum [2]: the mPIE allows the object (and probe) updates to progress without the addition of momentum for a fixed number of cycles, T. When momentum is to be applied, the first step is to update a velocity map, v_{ix}, based on the current object estimate and the object estimated stored immediately after the $(j\text{-}T)^{\text{th}}$ update:

$$v_{jx} = \eta_{obj} v_{(j-T)x} + \left(\mathbf{O}'_{jx} - \mathbf{O}_{(j+1-T)x} \right) \tag{S11}$$

where $v_{0x} = 0$, and $0 \le \eta_{obj} < 1$. Add a momentum to the j_{th} updated object estimate:

$$\mathbf{O}_{(j+1)x} = \mathbf{O}'_{jx} + \eta_{obj} v_{jx} \tag{S12}$$

10) Repeat steps 3-9 until all scanning shifts $\boldsymbol{R}_j$ have been traversed and an iteration has been completed.

11) Repeat N iterations until algorithm converges.

3. The detailed information about the home-built PMMI apparatus

Figure 2(a) illustrate our home-built PMMI apparatus on an optical bench, which is composed of a laser, a polarizer, a compensator, a lens, a sample, an analyzer and a detector. This configuration allows for the determination of only the first three rows of the Mueller matrix. While it is theoretically possible to retrieve all 16 Mueller elements by replacing the PSA with a rotating compensator and a fixed analyzer, the compensator in the PSA of the PMMI should be a wide field-of-view one to accommodate the cone beam, which would significantly increase the system complexity. Therefore, in this stage, we use a simplified experimental configuration for partial 3×4 Mueller matrix measurement.

For the laser, we chose the compact laser module (Thorlabs, PL202) with a center wavelength of 633nm. The light emitted from the laser passes through a nanoparticle liner film polarizer (Thorlabs, LPVISC100-MP2) which has a high extinction ratio and a thin thickness. Then the light passes through a polymer zero-order quarter-wave plate (Thorlabs, WPQ10ME-633) to be modulated into elliptically polarized light. True zero order wave plate provides stable performance over a large range of angles of incidence (AOI). After that, a plano-convex lens focused the light into a probe of hundreds of microns, facilitating the interaction with the sample. The diffracted field is demodulated by an analyzer (Thorlabs, LPVISE200-A) and recorded by a detector (QHYCCD, QHY268M) with a pixel size of 3.76 μm × 3.76 μm and a resolution of 6280 ×4210 pixels. For data processing, only the central 4096 ×4096 pixels are used. A liner stage (PI, M-L01.2S0) moves the sample to complete the scan. Note that on the one hand, the diameter of the analyzer is 2 inches, twice that of the polarizer, on the other hand the analyzer has an acceptance incidence angle of ±30°, ensuring uniform modulation of all diffracted light. The quarter-wave plate and analyzer are mounted on the manual high-precision rotation mounts (PRM1/M and PRM2/M), enabling adjustment to various azimuth angles. The sample is scanned under each polarization state, generating a series of diffraction fields. In the experiments described in the main text, considering both the solvability and measurement efficiency of the Mueller matrix, the number of PSG states and PSA states is set to 4. The quarter-wave plate in the PSG was rotated to four different angles (0°, 20°, 40°, 60°), and the analyzer in the PSA was also rotated to four different angles (0°, 45°, 90°, 135°), generating a total of 16 polarization combinations. In this work, the 'HUST' sample has dimensions of 440 μm × 440 μm. To cover the whole pattern, the probe is set to approximately 200 μm, with a scanning step of 20 μm, following a scanning trajectory of 14 × 14. A single ptychographic imaging requires approximately 13 minutes to complete, and with 16 polarization states, a total of 16 scans are necessary. Consequently, it takes about 208 minutes to perform a complete PMMI of the 'HUST' sample.

4. The detailed information about the customized birefringent specimen

The specimen features the acronym 'HUST' in the central square region, representing Huazhong University of Science and Technology. Additionally, two columns of numbers,

‘1952’ on the left and ‘2024’ and right, symbolize the historical timeline of HUST. At the top of the specimen, the pattern ‘NOM’ represents the Nanoscale and Optical Metrology Research Center., while the pattern ‘MSE’ at the bottom stands for the School of Mechanical Science and Engineering of HUST. The size of the specimen is approximately 440 μm × 440 μm. The designed retardance for the whole specimen is 180° for 633nm wavelength. The designed axis azimuths are as follows:120°,150°,0° and 30° for ‘H’, ‘U’, ‘S’, and ‘T’; 120°,150°,0° and 30° for ‘1’, ‘9’, ‘5’, and ‘2’; 120°,150°,0° and 30° for ‘2’, ‘0’, ‘2’, and ‘4’; 120° for ‘N’, ‘O’, and ‘M’; 30° for ‘M’, ‘S’, and ‘E’; 90° for the inner square background and outer background; 135° for the middle background.

Fig. S4 shows the sixteen reconstructed polarization-modulated amplitudes of the specimen by mPIE.

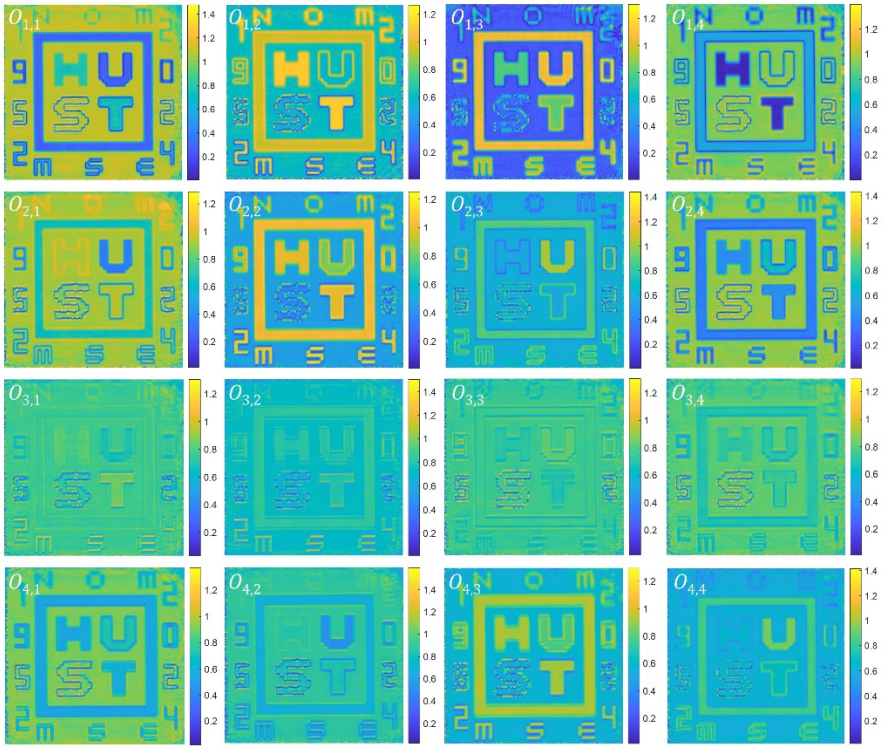

Fig. S4. Sixteen reconstructed polarization-modulated amplitudes of the customized birefrigent specimen by mPIE.

References

1. L. Liu, W. Li, M. Gong, L. Zhong, H. Gu and S. Liu, "Resolution Enhanced Lensless Ptychographic Microscope Based on MaximumLikelihood High-Dynamic-Range Image Fusion," IEEE Trans. Instrum. Meas. **73**, 1-11, 2024
2. A. Maiden, D. Johnson, and P. Li, “Further improvements to the ptychographical iterative engine,” Optica **4** (7), 736-745 (2017)